Progress In Electromagnetics Research C, Vol. 111, 225–239, 2021

Comparative Design and Analysis of a New Type of Mechanical-Variable-Flux Flux-Intensifying Interior Permanent Magnet Motor

Xiping Liu, Gaosheng Guo*, Wenjian Zhu, and Longxin Du

Abstract—In this paper, a novel mechanical-variable-flux flux-intensifying interior permanent magnet (MVF-FI-IPM) motor is proposed, which employs a mechanical flux-adjusting device and owns the characteristic of $L_d > L_q$. The magnetic poles can be rotated by the mechanical device to vary the leakage flux and adjust the angle of magnetization direction relative to the d-axis. The characteristic of $L_d > L_q$ is achieved through the adoption of surface flux barriers. The topology structure and operation principle of the machine are introduced. Then, the operation of the mechanical flux-adjusting device is analyzed by virtual prototype technology. Based on the two-dimensional finite element method (FEM), the electromagnetic characteristics of the proposed motor and FI-IPM motor are compared. Finally, the results show the proposed motor with a better flux-weakening capability and a lower risk of irreversible demagnetization than that of the FI-IPM motor.

1. INTRODUCTION

Permanent magnet synchronous machines (PMSMs) offer significant advantages such as high efficiency, high torque-to-current ratio, high torque-to-volume ratio, and high power factor, thus PMSM is widely and successfully used in electric vehicles (EV), hybrid electric vehicles (HEVs), electric aircraft, and industrial application [1–3]. Nevertheless, the air-gap magnetic field of the conventional PM machine is difficult to regulate, which leads to limited constant-power speed range (CPSR) [4, 5]. Generally, the conventional PM machines utilize the negative d-axis flux-weakening current to extended CPSR, but the efficiency of PMSM is low under high-speed operation, which results from the larger flux-weakening current. Besides, the flux weakening method increases the risk of PM irreversible demagnetization [6–8]. To solve those situations, many scholars and research institute researches study PMSMs.

In the past few years, some valid methods have been proposed to achieve a wider speed range. In [9], flux-intensifying interior permanent magnet (FI-IPM) motors are proposed. The FI-IPM machine possesses the unique characteristic of the d-axis inductance L_d larger than that of the q-axis inductance L_q extended operation speed range [10–12]. The characteristic enables the FI-IPM motor to obtain a positive reluctance torque at a positive d-axis current, which means the maximum torque of the FI-IPM motor operation on flux intensifying range. Compared with the maximum torque of conventional interior PM motor under negative i_d, the risk of irreversible demagnetization can be reduced [13, 14]. To realize the characteristic of $L_d > L_q$, the primary method is to increase L_d and reduce L_q. A few methods are briefly described below: the first method, to achieve the characteristic, adopts design multiple flux barriers on the q-axis rotor topology [15–17], and the method can greatly reduce L_q, but it will affect the mechanical strength and torque ripple of the motor [18]; the second method is to use the q-axis barriers and magnetic bridges to reduce L_q and increase L_d [14], and the method can realize

Received 23 February 2021, Accepted 26 March 2021, Scheduled 9 April 2021
* Corresponding author: Gaosheng Guo (1400681644@qq.com).
The authors are with the School of Electrical and Automation, Jiangxi University of Science and Technology, Ganzhou, China.

preferable flux-intensifying effect; the third method is to adopt a nonuniform air-gap on the surface of the rotor [19, 20], so the magnetic reluctance air barrier is added to the q axis magnet path to reduce L_q. Compared to other methods, the third method is easier to realize $L_d > L_q$ and can obtain better flux-intensifying effect and torque characteristics, so the method is applied to the proposed motor. In [21, 22], a mechanical variable flux (MVF) motor is proposed, and the rotor of the machine is equipped with a flux-adjusting device to reduce the air-gap flux, thus extend the CPSR. The flux-adjusting device is driven by centrifugal force [23], thus the weakening current is greatly reduced, which means that the loss of the machine can be reduced by the device.

In this paper, a novel MVF-FI-IPM motor is proposed. The MVF-FI-IPM motor combines the advantages of the FI-IPM motor and MVF motor, which own a unique characteristic of $L_d > L_q$ and equip with an additional mechanical flux-adjusting device. So the flux-weakening ability of the proposed motor can be improved. The configuration and operation principle of the machine are introduced. The mechanical dynamics characteristics of the mechanical flux-adjusting device are analyzed by the 3D automatic dynamic analysis of mechanical system (ADAMS). Besides, the electromagnetic performances of the proposed motor and FI-IPM motor are compared by FEM, including the performance of the torque and inductance, flux-weakening capability, and demagnetization risk of PMs. Finally, it is confirmed that the performance of the proposed motor is better.

2. MODELING

2.1. Topology Structure of the Machine

In this paper, a FI-IPM motor is selected as the comparison motor. The stator structure and winding mode of the two motors are the same, and the rotor structure is similar. The major differences between these two machines lie in the structure of PMs, and the rotor of the proposed machine is equipped with a mechanical flux-adjusting device. Figure 1 shows the topology structure of the two motors.

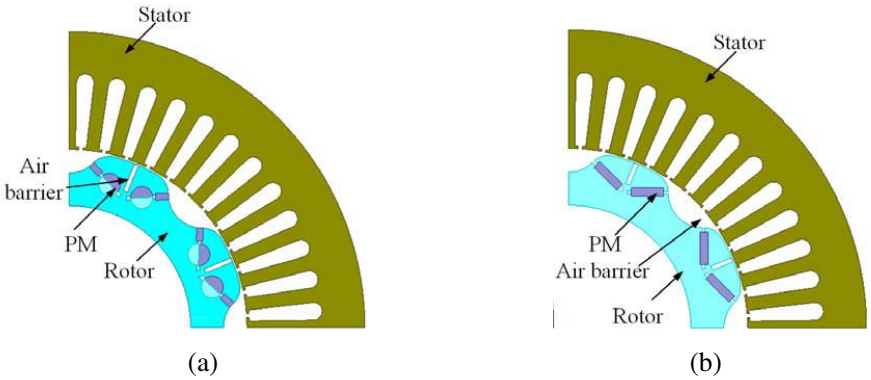

Figure 1. Configurations of the two motors. (a) MVF-FI-IPM motor. (b) FI-IPM motor.

In the MVF-FI-IPM motor, the stator adopts 48 slots with integral slot distributed windings, and the rotor has a larger q-axis magnetic reluctance by the adoption of nonuniform air-gap; thus, L_q is reduced. Besides, to reduce the d-axis inductance, the cylinder is divided into two parts, in which one part is PM, and the other part is magnetic material. Consequently, the proposed motor can realize the characteristic of $L_d > L_q$. The PM structure is composed of a rectangle shape and cylinder shape. The cylinder shape of PM is connected with the mechanical device by a connecting rod. The key parameters of the two motors are given in Table 1.

2.2. Topology Structure of the Mechanical Device

In Figure 2, the topology structure of the mechanical flux-adjusting device is shown. It can be observed that the device mainly consists of disc, spring, sliding block, bring gear, and connecting rod. The device

Table 1. Key parameters of the two motors.

Items	Value
Rated power (kW)	1
Rated voltage (V)	25
Rated speed (rpm)	700
Stator outer diameter (mm)	269.6
Rotor outer diameter (mm)	160.4
Air-gap length (mm)	0.75
Turn numbers	10
Number of slots/pole	48/8
Stack length (mm)	40
PM type	N38UH (1.04 T, 580 kA/m)
Volume of PM (mm^3)	$110 * 40 * 8$

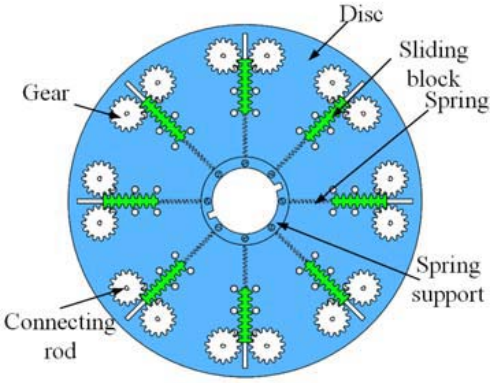

Figure 2. Structure of mechanical flux-adjusting device.

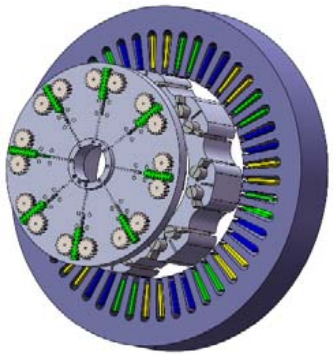

Figure 3. Three-dimensional explosion diagram.

is installed on the rotor by the rotating shaft. Design the sliding chutes on the disc, which can restrict the moving range of the sliding block. The sliding block is connected to the disc by spring, thus the movement of the sliding block is limited. Besides, the sliding friction of the sliding block is changed to rolling friction by mounting the bearings inside the disc, which greatly reduces the effect of friction. The gear is connected to the cylinder shape PM through the connecting rod, thus the PM can be controlled by the mechanical device. When the rotational speed reaches above the base speed, the centrifugal force of the slider is greater than the prestress of the spring, thus the slider starts to move along the chute to drive the gear rotation. The device is driven by centrifugal force, which establishes a relationship between magnetic field strength and velocity. The overall three-dimensional explosion diagram of the machine is shown in Figure 3.

3. OPERATION PRINCIPLE OF MACHINE

3.1. The Principle of the Mechanical Flux-Adjust Device

The mechanical flux-adjust device is an important part of the MVF-FI-IPM motor. The flux weakening ability of the proposed motor has been greatly improved to extend the speed range by adopting the mechanical flux-adjusting device. Therefore, the analysis of the operating principle of mechanical device is essential.

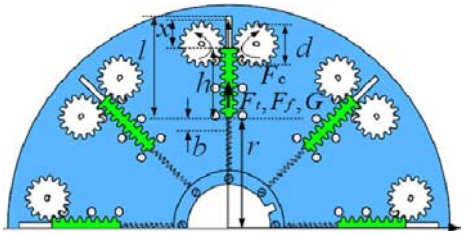

Figure 4. Force analysis for the sliding block.

For analyzing the dynamic operation of the mechanical device, the force analysis of the sliding block is shown in Figure 4. The displacement between the slider and the gear has the following relationship:

$$x = \frac{a}{360} d\pi \tag{1}$$

where x is the displacement length of the sliding block; α, d are the rotation angle and diameter of the gear.

The radial force of the sliding block is mainly considered. The sliding block is subject to five forces: (i) self-gravity G; (ii) the supporting force of the disc F_N; (iii) the fraction F_f because of contact with sliding chute; (iv) the spring tension force F_t; (v) the centrifugal force F_c due to the rotation of the rotor. Assume that the sliding block and disc surfaces are smooth enough, thus F_f can be ignored. Besides, G accounts for 3% of centrifugal force at rated speed, so G can also be neglected.

The spring tension calculation equation is as follows:

$$F_t = kx + F_p \tag{2}$$

where k is the spring constant, and F_p is the prestressing force of the spring.

The mechanical device is mounted on the rotor and rotates together with the rotor. So the centrifugal force is generated and calculated by the following equation.

$$F_c = mw^2 \left(r + x + \frac{h}{2} \right) \tag{3}$$

where m is the mass of the sliding block, w the angular velocity of the rotor, r the distance from the bottom of the chute to the center of the disc, and h the length of the sliding block.

There are two operation states of the sliding block, i.e., below the speed and above the base speed which are shown in Figure 5. The force analysis can be expressed as follows:

$$F_c = \begin{cases} F_t - F_N, & (w < w_r) \\ F_t, & (w \geq w_r) \end{cases} \tag{4}$$

where w_r is the rated angular velocity of the motor.

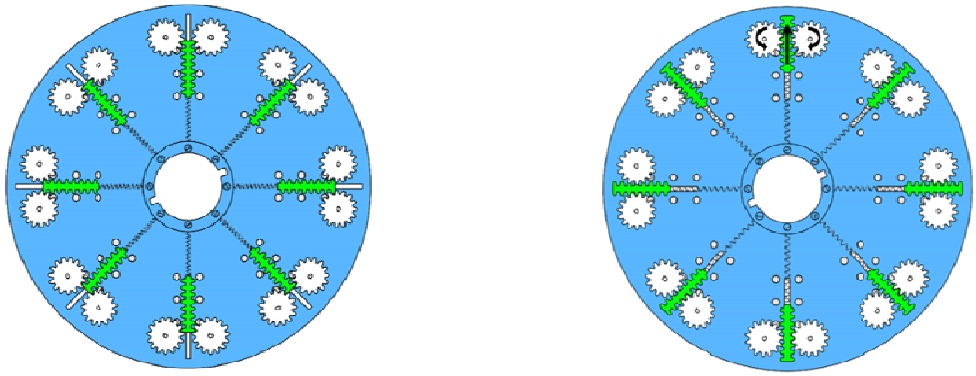

(a) (b)

Figure 5. Operation of the sliding block. (a) Below the base speed. (b) Above the base speed.

3.2. The Operation Principle of Motor

The maximum angular speed $w_{\max}$ of PMSM can be expressed as below:

$$w_{\max} = \frac{U_{\lim}}{p(\psi_f - L_d I_{\lim})} \tag{5}$$

where $U_{\lim}$ and $I_{\lim}$ are the limiting voltage and current; p and ψ_f are pairs and flux linkage of PMs.

According to Eq. (5), there are limits to the voltage and current caused by the inverter. Therefore, when the voltage and current reach the limit values, the wider speed range of the motor can be realized by decreasing the PM flux linkage and increasing the d-axis inductance. The following is an analysis of the operation principle.

The flux-adjusting principle of the proposed motor is shown in Figure 6(a). As seen from the figure, as the rotation angle α increases, the variation of the permanent magnet can be regarded as the magnetization direction of the permanent magnet rotating from the inside to the outside, thus the component of the PM in the d-axis is decreased. The magnetic field line distribution of the proposed motor under different rotation angles is shown in Figure 6(b). It can be seen that the leakage flux of PMs increases with the increase of the rotation angle. It means that the flux-weakening ability of the proposed motor increases with the increase of rotation speed.

For further analysis of the operation principle of the proposed motor, the stator armature voltage of the proposed motor in the d-q reference in the dynamic state and the magnetic flux linkage calculation are expressed by Eqs. (6) and (7), respectively.

$$\begin{cases} u_d = R_w i_d + \dfrac{d\psi_d}{dt} - w\psi_q \\ u_q = R_w i_q + \dfrac{d\psi_q}{dt} - w\psi_d \end{cases} \tag{6}$$

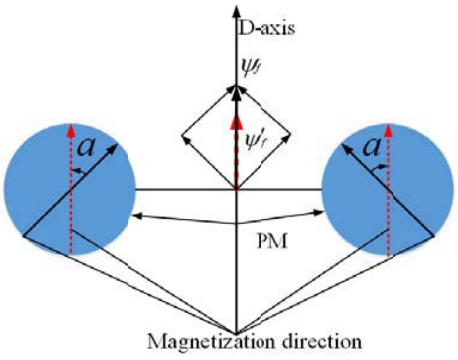

(a)

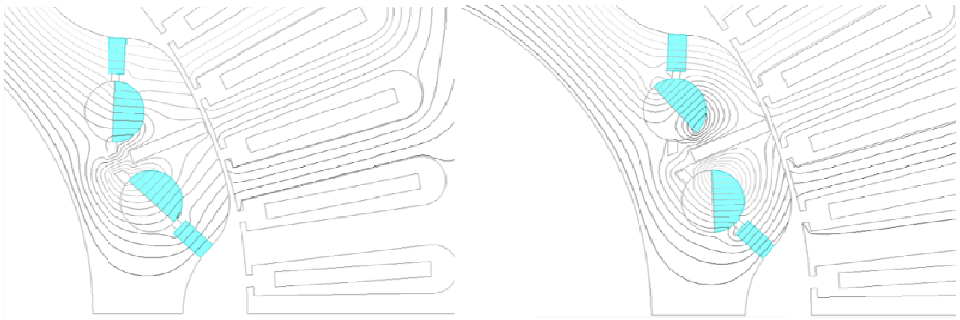

(b)

Figure 6. The operation principle of the MVF-FI-IPM motor. (a) Flux-adjusting principle of the MVF-FI-IPM motor. (b) The magnetic field line distributions with different rotation angles.

$$\begin{cases} \psi_d = \psi_{pm} + L_d i_d \\ \psi_q = L_q i_q \end{cases} \tag{7}$$

where u_d and u_q are the d-axis and q-axis armature voltages; i_d and i_q are the d-axis and q-axis armature currents; λ_d and λ_q are the d-axis and q-axis flux linkages; R_w is the resistance of the winding. Among them, ψ_f and L_d are affected by the rotation angle α. Therefore, the flux linkages can also be expressed as follows:

$$\begin{cases} \psi_d = \psi_d(i_d, i_q, \alpha) \\ \psi_q = \psi_q(i_d, i_q, \alpha) \end{cases} \tag{8}$$

$$\begin{cases} \dfrac{d\psi_d}{dt} = \dfrac{\partial \psi_d}{\partial i_d}\dfrac{\partial i_d}{\partial t} + \dfrac{\partial \psi_d}{\partial i_q}\dfrac{\partial i_q}{\partial t} + \dfrac{\partial \psi_d}{\partial \alpha}\dfrac{\partial \alpha}{\partial t} \\ \dfrac{d\psi_q}{dt} = \dfrac{\partial \psi_q}{\partial i_d}\dfrac{\partial i_q}{\partial t} + \dfrac{\partial \psi_q}{\partial i_q}\dfrac{\partial i_q}{\partial t} + \dfrac{\partial \psi_q}{\partial \alpha}\dfrac{\partial \alpha}{\partial t} \end{cases} \tag{9}$$

The two motors own the unique characteristic of $L_d > L_q$. To clarify the flux-intensifying effect, the flux paths of the d-axis and q-axis and the corresponding equivalent magnetic circuits are illustrated in Figure 7. Based on the magnetic circuits, L_d and L_q can be expressed as below:

$$\begin{cases} L_d = \dfrac{N^2}{R_s + R_r + 2(R_{pm}R_l/(R_{pm} + R_l) + R_{air})} \\ L_q = \dfrac{N^2}{R_s + R_r + 2(R_{air} + R_b)} \end{cases} \tag{10}$$

where N is the number of turns of winding; the reluctances of stator, rotor, air-gap, air barrier, PM are R_s, R_r, R_{air}, R_b, R_{pm}, respectively; R_l is the reluctance of leakage flux of path. The leakage flux of the FI-IPM is very low, so the leakage flux loop of the FI-IPM can be ignored (i.e., R_l is infinite).

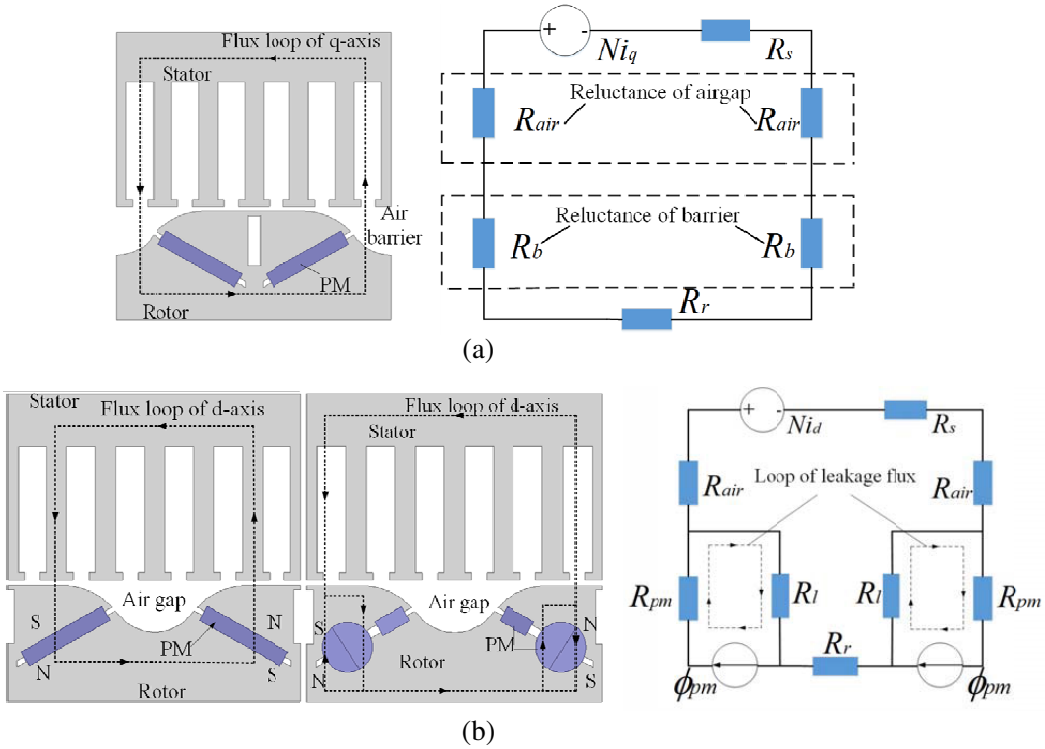

Figure 7. Flux path of the two motors. (a) q-axis flux path. (b) d-axis flux path.

4. MECHANICAL DEVICE DYNAMICS ANALYSIS

In order to verify the reliability of the mechanical flux-adjusting device, the dynamic analysis of the device is carried out by using the virtual prototype software of ADAMS. The 3D virtual prototype model of the mechanical device is shown in Figure 8, where the model is simplified and only retained on the assembly unit to improve the simulation efficiency. The key parameters and specific constraints of the device are listed in Tables 2 and 3, respectively.

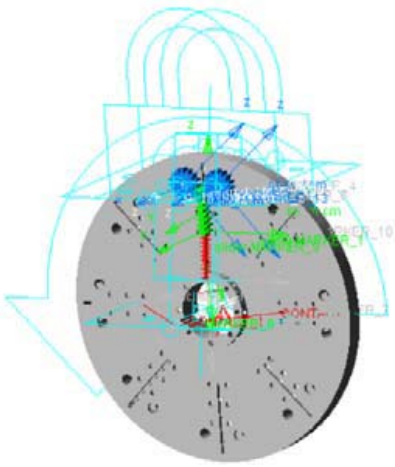

Figure 8. Virtual prototype model.

Table 2. Key parameters of the mechanical device.

Parameters	Unit	Value
Single sliding block mass, m	kg	0.02
Length of sliding chute, l	mm	37.5
Spring constant, k	N/mm	4.26
Radius at block rest position, r	mm	39.5
Gear graduated circle diameter, d	mm	15
Spring pre-load, F_{e0}	N	5.58

Table 3. The constraint relation relationship between the components of flux-adjusting device.

Constrain	Component 1	Component 2
Revolute joint	Disc	ground
Translational joint	Sliding block	Disc
Revolute joint	Gear	Disc
Flexible connection	Sliding block	Disc
Contact	Sliding block	gear

The main material of the mechanical device is copper, which is to avoid leakage flux between the rotor and the device. By setting an acceleration of the mechanical, the operating state of the device at different speeds is shown in Figure 9. The relationship between acceleration and speed is shown in Figure 9(a). From 0 to 1 sec, the virtual prototyping model steadily accelerates to 2000 r/min with the

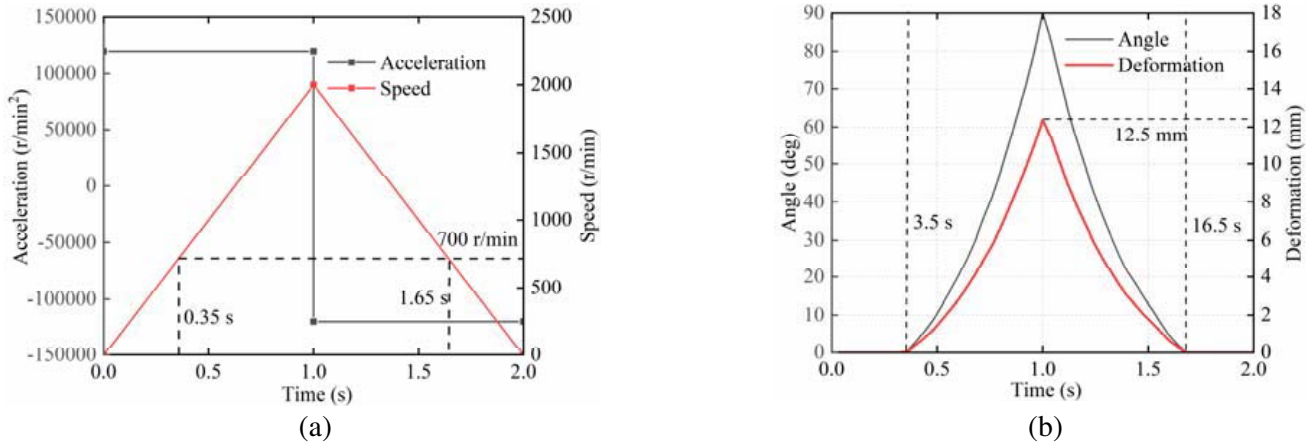

Figure 9. Analysis of the mechanical flux-adjust device. (a) Relationship between acceleration and speed. (b) Relationship between deformation and the rotation angle.

acceleration of 120000 r/min^2, then it steadily decelerates to 0 with the acceleration of -120000 r/min^2 from 1 to 2 sec. The deformation of the spring and the rotation angle of the gear is shown in Figure 9(b). It can be seen that the spring begins to deform, and the gear starts to rotate at 0.35 sec (i.e., speed = 700 rpm), which is the result of prestressing. As the speed increases, the deformation of the spring and rotation angle of the gear increase rapidly because the centrifugal force is proportional to the square of the velocity. When speeding is up to 2000 rpm (i.e., $t = 1$ s), the deformation of the spring is 12.5 mm, and the rotation angle of gear is 90 deg. The spring deformation is limited by the sliding chute. Therefore, when the slider reaches the top of the chute, the permanent magnets no longer rotate, and the flux weakening capability of the proposed motor reaches maximum.

5. ELECTROMAGNETIC PERFORMANCES ANALYSIS

5.1. No-Load Back-EMF

Figure 10(a) shows the no-load back-EMF waveforms of the two motors at the speed of 600 rpm. The slider of the proposed motor does not move, and the rotation angle of PM is 0 deg because of the prestress. It can be observed that the back-EFM of the proposed motor and FI-IPM are almost the same. It means that the two motors possess the same magnetic load. Moreover, the Fast Fourier

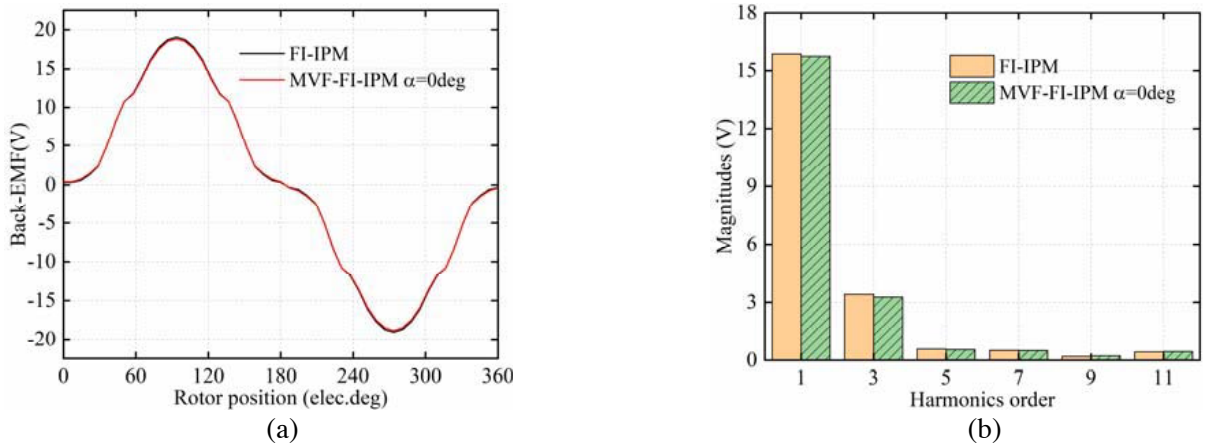

Figure 10. No-load back EFM of the two motors. (a) Waveforms. (b) Harmonics components.

Transform (FFT) analysis results are shown in Figure 10(b). From the figure, the harmonic percentage composition of each order is the same.

5.2. Inductance Characteristics

The analysis of inductance characteristics is essential, and the inductance has a significant influence on the flux weakening capability, especially for the FI-IPM motor.

Figure 11 depicts L_d and L_q under the no-load. It can be found that the q-axis inductances of the two motors have almost the same value. However, L_d of the proposed motor is larger than that of the FI-IPM motor, which results from the unique PM structure of the proposed motor. In addition, it can be seen that both of the motors own the unique characteristic of $L_d > L_q$.

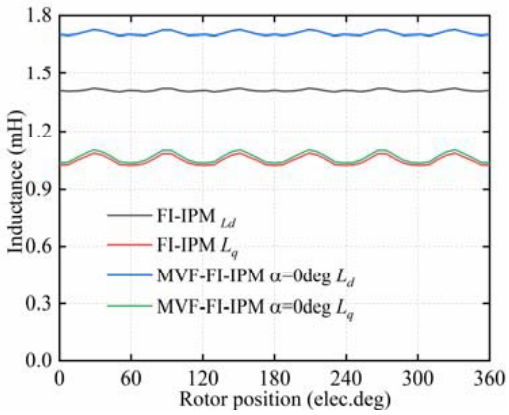

Figure 11. Characteristics of inductance versus rotor position.

The inductance characteristics of the two motors under different current conditions are shown in Figure 12, where the current angle is zero, and the current varies from 0 A to 80 A. It can be found that the inductance of the two motors changes very little with the current increasing. It indicates that the two motors can effectively avoid cross-coupling magnetic saturation.

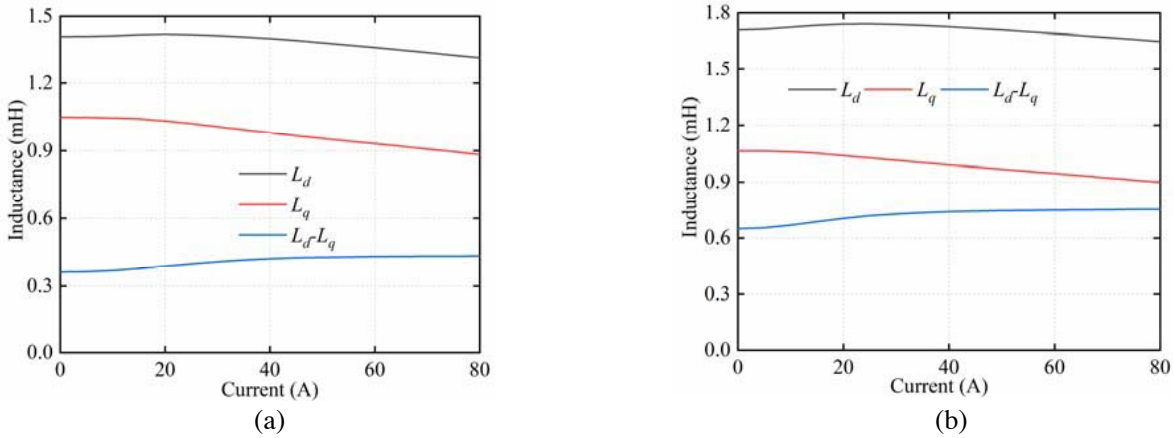

Figure 12. Inductance variation characteristics of the two motors. (a) Variation of inductance with the current in FI-IPM machine. (b) Variation of inductance with the current in MVF-FI-IPM. machine.

In the above analysis, the mechanical device of the proposed motor is not running, which means that the rotation angle of the permanent magnet is zero. Therefore, the inductance of the proposed motor will be investigated under the operation of mechanical device. Figure 13 shows the inductance

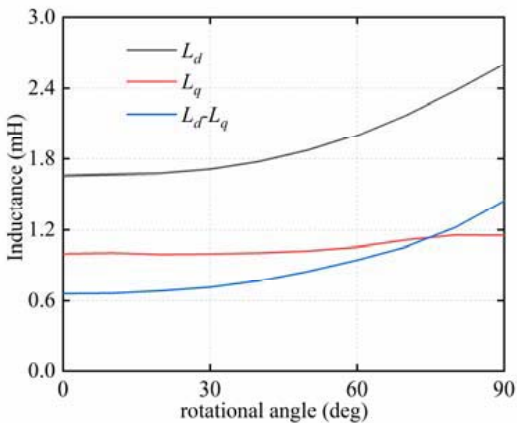

Figure 13. Variation of inductance with the rotational angle in MVF-FI-IPM machine.

characteristic of the proposed motor under different rotation angles of the PM. From the figure, it can be observed that the q-axis inductance of the proposed motor is less sensitive to the rotation angle, but the d-axis inductance varies largely with the increased rotational angle. As the angle increases, the leakage flux of the permanent magnet gradually increases, and the magnetic field strength decreases, thus the d-axis magnetoresistance decreases. The flux weakening ability of the proposed motor will be improved with the increase of the difference between L_d and L_q.

5.3. Torque Characteristics

The torque performances of the two motors under different current angles are shown in Figure 14. The maximum torque of the two motors is reached at the positive d-axis current due to $L_d > L_q$. It can be seen that the maximum torques of the FI-IPM motor and MVF-FI-IPM motor ($\alpha = 0\,\text{deg}$) are almost the same. Moreover, it is also noted that the flux-intensifying performance of the proposed motor is slightly higher than that of the FI-IPM motor, due to the bigger difference between L_d and L_q. As the rotation angle of PM increases, the torque of the proposed motor is reduced, and the maximum torque is reached at a smaller current angle due to the increase of the difference between L_d and L_q.

In Figure 15, the cogging torque waveforms of the two proposed motors are compared. It can be found that the cogging torque of the FI-IPM is slightly larger than that of the MVF-FI-IPM ($\alpha = 0\,\text{deg}$), and the cogging torque of the proposed motor decreases with the increase of the rotation angle of PM.

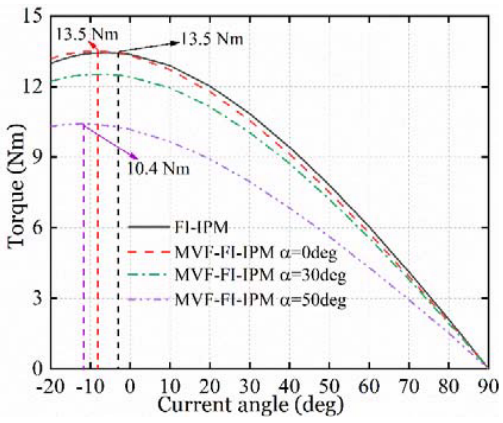

Figure 14. Torque characteristics of the FI-IPM and MVF-FI-IPM machine.

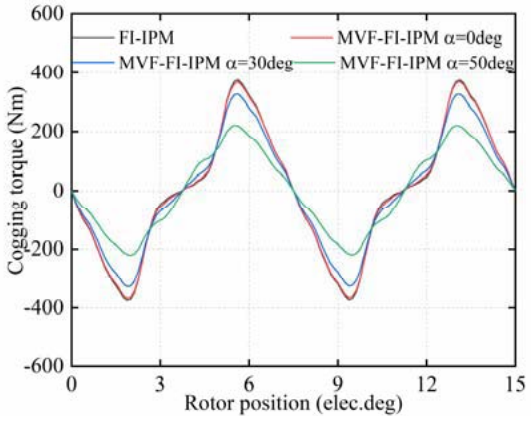

Figure 15. Cogging torque of the FI-IPM and MVF-FI-IPM machine.

5.4. Flux-Weakening Ability and Speed Range

The analysis of the speed range is essential to evaluating the performance of the motor. Therefore, it is necessary to research the flux-weakening ability.

The air-gap flux density of the two motors under no-load condition is shown in Figure 16, where rotation angles of PM of the proposed motor are selected at 0 deg, 30 deg, and 50 deg. It can be found that the air-gap flux density of the FI-IPM motor is slightly higher than that of the proposed motor ($\alpha = 0$ deg). Furthermore, the air-gap flux density of the MVF-FI-IPM motor under $\alpha = 50$ deg is significantly less than the MVF-FI-IPM under $\alpha = 0$ deg. It means that the flux density of the proposed motor can be efficiently decreased by the mechanical flux-adjusting device to rotate the PMs.

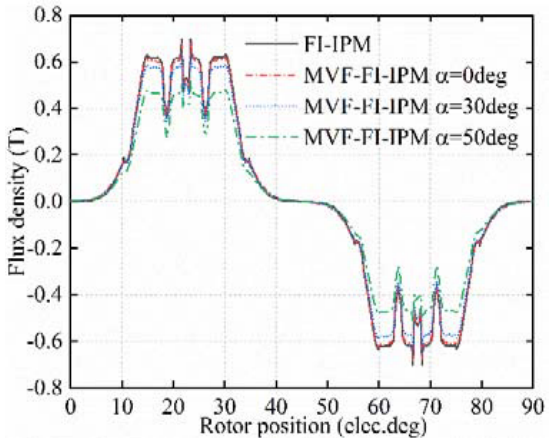

Figure 16. The air flux density of the FI-IPM and MVF-FI-IPM machine.

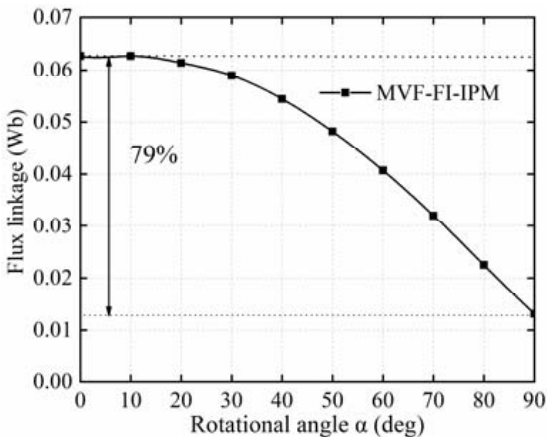

Figure 17. Variation of flux linkage with the rotational angle in MVF-FI-IPM machine.

The flux linkage of the proposed motor under the different rotational angles of PM is shown in Figure 17. It can be found that the flux linkage decreases with the increase of rotation angle. The variable range of flux linkage is approximately 79%. The widely variable range of flux linkage can be obtained by adopting the mechanical device. It means that the flux-weakening capability of the proposed motor can be improved.

Figure 18 shows the torque-speed envelops and output power-speed envelops of the two motors, where the rated speed is 700 r/min. It can be observed that the speed range of the FI-IPM motor is lower than the MVF-FI-IPM motor ($\alpha = 0$ deg), which mainly results from the relatively bigger difference

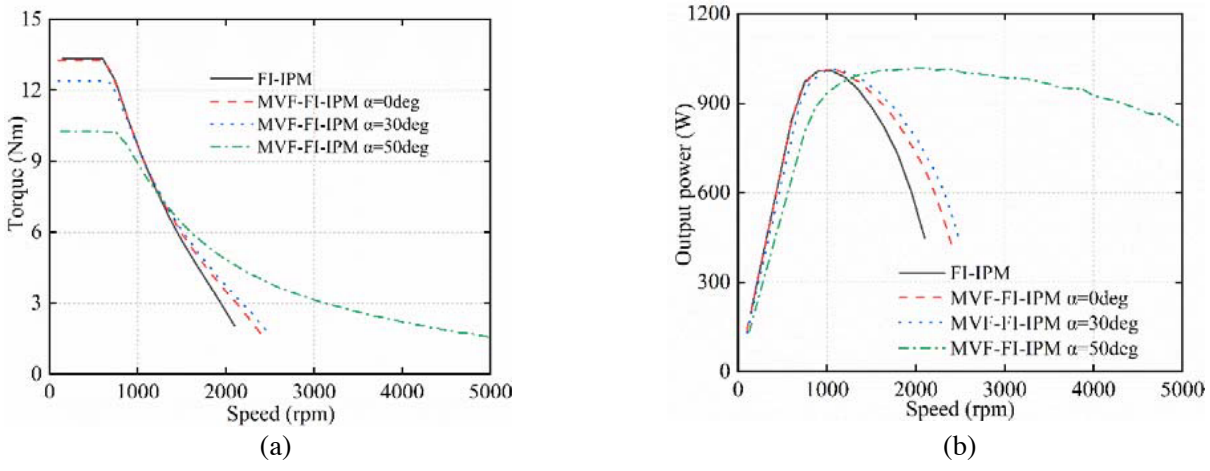

Figure 18. Performance comparisons of the two motors. (a) Torque-speed. (b) Power-speed envelops.

between L_d and L_q. Besides, the speed range of the MVF-FI-IPM motor increases sharply with the increase of the rotation angle of PM. It can be aware that the speed range of the proposed motor can be extended by the mechanical device.

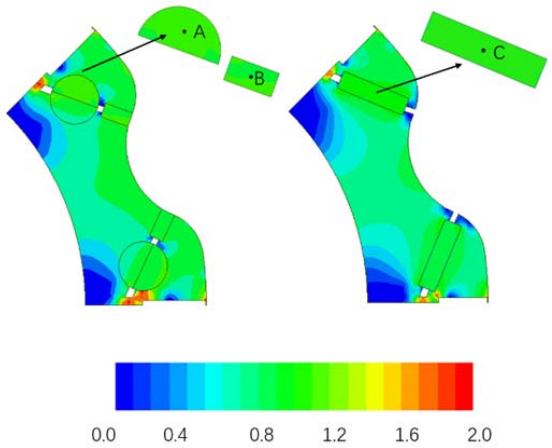

Figure 19. The flux density distributions at the maximum torque.

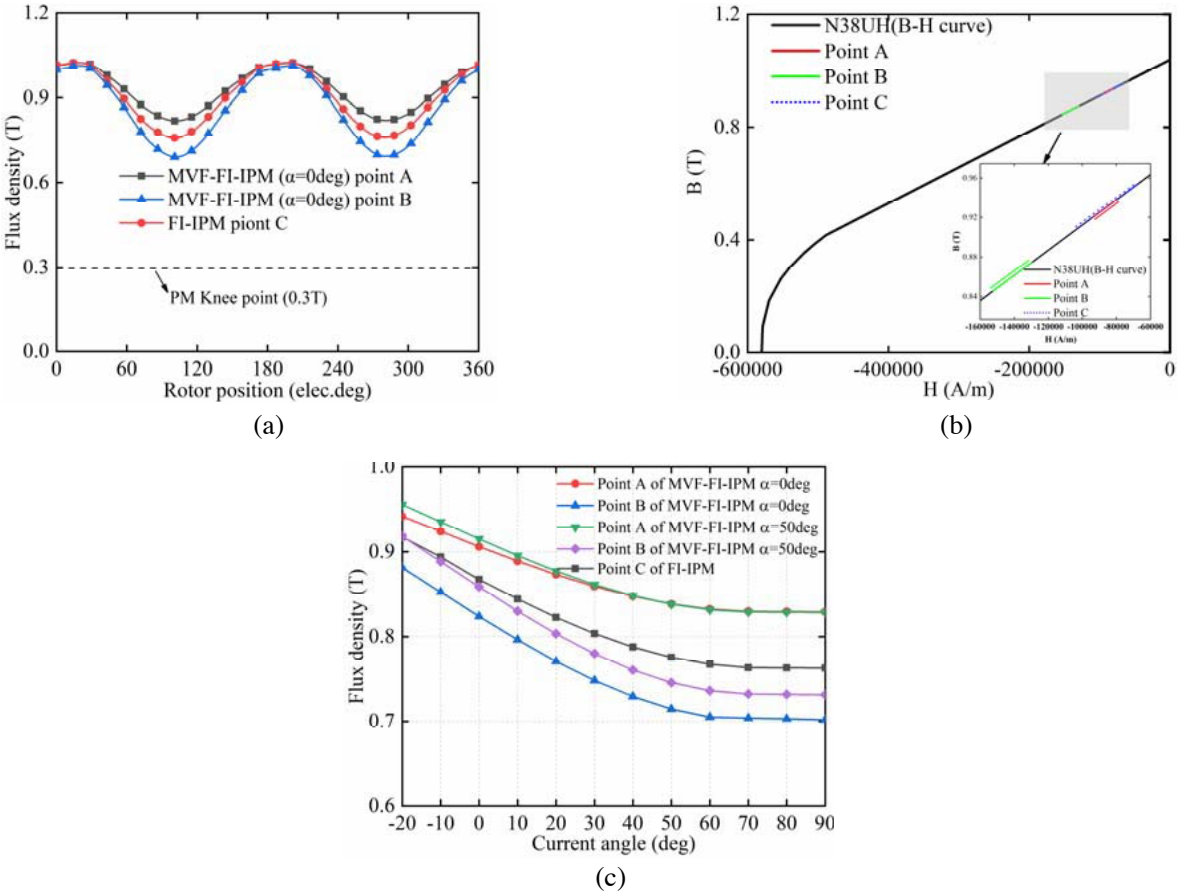

Figure 20. Analysis of the irreversible demagnetization risk of the two motors. (a) Flux density variation of observation PM points of the two motors at different rotor positions. (b) Operating point range. (c) Variation of flux density versus current angle.

5.5. Evaluating the Irreversible Demagnetization Risk

The irreversible demagnetization risk of PM has a great influence on the performance of the motor. Therefore, the demagnetization evaluation of the PM cannot be ignored. In this section, the irreversible demagnetization risk of PMs is evaluated by finite element analysis method. In Figure 19, the flux density distributions of the two motors are shown, with the current of 25 A and speed of 700 rpm. To better analyze the magnetization state of the permanent magnet, three observed points are selected on the PMs.

Figure 20(a) displays the flux density of the three observed points under different rotor positions. From the figure, it can be seen that the flux density of point A is relatively larger than that of other points. It is also noted that the flux density of the three observed points is higher than that of the knee point of the PM because the two motors possess unique characteristics of $L_d > L_q$. Moreover, the operating range of the three observed points is shown in Figure 20(b). The variation of the flux density of the three observed points under different current angles is depicted in Figure 20(c). The flux density of the three observed points decreases as the current angle increases, but the flux densities of the PMs of the two motors are still much larger than the threshold value of PM (i.e., 0.3 T). In addition, the flux densities of point A and point B increase with the increase of the rotation angle due to the flux intensifying effect. It means that the lower risk of irreversible demagnetization of the proposed motor can be obtained.

6. CONCLUSION

In this paper, a novel MVF-FI-IPM motor with the characteristic of $L_d > L_q$ and a mechanical flux-adjusting device is proposed. The electromagnetic performances of the FI-IPM motor and MVF-FI-IPM motor are evaluated, which indicates that the proposed motor has a better flux-intensifying effect, excellent flux-weakening capability, lower risk of irreversible demagnetization.

REFERENCES

1. Wang, D., X. Wang, and S.-Y. Jung, "Cogging torque minimization and torque ripple suppression in surface-mounted permanent magnet synchronous machines using different magnet widths," *IEEE Transactions on Magnetics*, Vol. 49, No. 5, 2295–2298, 2013.
2. Chen, Q., G. Xu, F. Zhai, and G. Liu, "A novel Spoke-type PM motor with auxiliary salient poles for low torque pulsation," *IEEE Transactions on Industrial Electronics*, Vol. 67, No. 6, 4762–4773, 2020.
3. Liu, F., L. Cheng, M. Wang, G. Qiao, P. Zheng, and H. Yang, "Comparative study of hybrid-PM variable-flux machines with different series PM configurations," *AIP Advances*, Vol. 9, No. 12, 19–25, 2019.
4. Afinowi, I. A. A., Z. Q. Zhu, Y. Guan, J. C. Mipo, and P. Farah, "Switched-flux machines with hybrid NdFeB and ferrite magnets," *Compel the International Journal for Computation and Mathematics in Electrical and Electronic Engineering*, Vol. 35, No. 2, 456–472, 2016.
5. Liu, X. P., M. Wang, D. Chen, and Q. H. Xie, "A variable flux axial field permanent magnet synchronous machine with a novel mechanical device," *IEEE Transactions on Magnetics*, Vol. 51, No. 11, 5876–5887, 2015.
6. Aljehaimi, A. M. and P. Pillay, "Operating envelopes of the variable-flux machine with positive reluctance torque," *IEEE Transactions on Transportation Electrification*, Vol. 4, No. 3, 707–719, 2018.
7. Ibrahim, M., L. Masisi, and P. Pillay, "Design of variable flux permanent-magnet machine for reduced inverter rating," *IEEE Transactions on Industry Applications*, Vol. 51, No. 5, 3666–3674, 2015.
8. Hua, H., Z. Q. Zhu, A. Pride, R. P. Deodhar, and T. Sasaki, "Comparison of end effect in series and parallel hybrid permanent-magnet variable-flux memory machines," *IEEE Transactions on Industry Applications*, Vol. 55, No. 3, 2529–2537, 2019.

9. Limsuwan, N., T. Kato, K. Akatsu, and R. D. Lorenz, "Design and evaluation of a variable-flux flux-intensifying interior permanent-magnet machine," *IEEE Transactions on Industry Applications*, Vol. 50, No. 2, 1015–1024, 2014.
10. Limsuwan, N., Y. Shibukawa, D. D. Reigosa, and R. D. Lorenz, "Novel design of flux-intensifying interior permanent magnet synchronous machine suitable for self-sensing control at very low speed and power conversion," *IEEE Transactions on Industry Applications*, Vol. 47, No. 5, 2004–2012, 2011.
11. Kato, T., N. Limsuwan, C. Y. Yu, K. Akatsu, and R. D. Lorenz, "Rare earth reduction using a novel variable magnetomotive force flux-intensified IPM machine," *IEEE Transactions on Industry Applications*, Vol. 50, No. 3, 1748–1756, 2014.
12. Liu, F. J., X. Y. Zhu, W. Y. Wu, L. Quan, Z. X. Xiang, and Y. Z. Hua, "Design and analysis of an interior permanent magnet synchronous machine with multiflux-barriers based on flux-intensifying effect," *IEEE Transactions on Applied Superconductivity*, Vol. 28, No. 3, 1949–1964, 2018.
13. Kim, K. C., K. Kim, H. J. Kim, and J. Lee, "Demagnetization analysis of permanent magnets according to rotor types of interior permanent magnet synchronous motor," *IEEE Transactions on Magnetics*, Vol. 45, No. 6, 2799–2802, 2009.
14. Zhao, X. K., B. Q. Kou, L. Zhang, and H. Q. Zhang, "Design and analysis of permanent magnets in a negative-salient permanent magnet synchronous motor," *IEEE Access*, Vol. 8, No. 54, 182249–182259, 2020.
15. Zhu, X. Y., W. Y. Wu, S. Yang, Z. X. Xiang, and L. Quan, "Comparative design and analysis of new type of flux-intensifying interior permanent magnet motors with different Q-axis rotor flux barriers," *IEEE Transactions on Energy Conversion*, Vol. 33, No. 4, 2260–2269, 2018.
16. Ngo, K., M. F. Hsieh, and A. Huynh, "Torque enhancement for a novel flux intensifying PMa-SynRM using surface-inset permanent magnet," *IEEE Transactions on Magnetics*, Vol. 55, No. 7, 253–260, 2019.
17. Sun, A., et al., "Magnetization and performance analysis of a variable-flux flux-intensifying interior permanent magnet machine," *2015 IEEE International Electric Machines & Drives Conference (IEMDC)*, 369–375, 2015.
18. Chen, J., J. Li, and R. Qu, "Maximum-torque-per-ampere and magnetization-state control of a variable-flux permanent magnet machine," *IEEE Transactions on Industrial Electronics*, Vol. 65, No. 2, 1158–1169, 2018.
19. Zhu, X., S. Yang, Y. Du, Z. Xiang, and L. Xu, "Electromagnetic performance analysis and verification of a new flux-intensifying permanent magnet brushless motor with two-layer segmented permanent magnets," *IEEE Transactions on Magnetics*, Vol. 52, No. 7, 1–4, 2016.
20. Zhang, L., X. Zhu, J. Gao, and Y. Mao, "Design and analysis of new five-phase flux-intensifying fault-tolerant interior-permanent-magnet motor for sensorless operation," *IEEE Transactions on Industrial Electronics*, Vol. 67, No. 7, 6055–6065, 2020.
21. Huang, C. Z., Z. X. Zhang, X. P. Liu, J. J. Xiao, and H. Xu, "Finite element analysis and dynamics simulation of mechanical flux-varying PM machines with auto-rotary PMs," *Journal of Power Electronics*, Vol. 19, No. 3, 744–750, 2019.
22. Liu, X., T. Sun, Y. Zou, C. Huang, and J. Liang, "Modelling and analysis of a novel mechanical-variable-flux IPM machine with rotatable magnetic poles," *IET Electric Power Applications*, Vol. 14, No. 11, 2171–2178, 2020.
23. Morimoto, E., N. Niguchi, and K. Hirata, "Variable flux permanent magnet motor utilizing centrifugal force," *International Journal of Applied Electromagnetics and Mechanics*, Vol. 52, Nos. 1–2, 563–569, 2016.